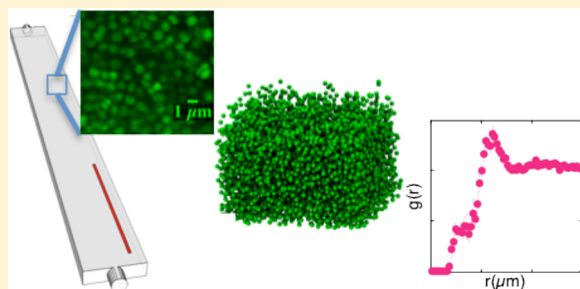


Role of Environmental and Antibiotic Stress on *Staphylococcus epidermidis* Biofilm MicrostructureElizabeth J. Stewart,<sup>†</sup> Ashley E. Satorius,<sup>‡</sup> John G. Younger,<sup>‡</sup> and Michael J. Solomon<sup>\*,†</sup>Departments of <sup>†</sup>Chemical Engineering and <sup>‡</sup>Emergency Medicine, University of Michigan, Ann Arbor, Michigan 48109, United States

## S Supporting Information

**ABSTRACT:** Cellular clustering and separation of *Staphylococcus epidermidis* surface adherent biofilms were found to depend significantly on both antibiotic and environmental stress present during growth under steady flow. Image analysis techniques common to colloidal science were applied to image volumes acquired with high-resolution confocal laser scanning microscopy to extract spatial positions of individual bacteria in volumes of size  $\sim 30 \times 30 \times 15 \mu\text{m}^3$ . The local number density, cluster distribution, and radial distribution function were determined at each condition by analyzing the statistics of the bacterial spatial positions. Environmental stressors of high osmotic pressure (776 mM NaCl) and sublethal antibiotic dose (1.9  $\mu\text{g/mL}$  vancomycin) decreased the average bacterial local number density 10-fold. Device-associated bacterial biofilms are frequently exposed to these environmental and antibiotic stressors while undergoing flow in the bloodstream. Characteristic density phenotypes associated with low, medium, and high local number densities were identified in unstressed *S. epidermidis* biofilms, while stressed biofilms contained medium- and low-density phenotypes. All biofilms exhibited clustering at length scales commensurate with cell division ( $\sim 1.0 \mu\text{m}$ ). However, density phenotypes differed in cellular connectivity at the scale of  $\sim 6 \mu\text{m}$ . On this scale, nearly all cells in the high- and medium-density phenotypes were connected into a single cluster with a structure characteristic of a densely packed disordered fluid. However, in the low-density phenotype, the number of clusters was greater, equal to 4% of the total number of cells, and structures were fractal in nature with  $d_f = 1.7 \pm 0.1$ . The work advances the understanding of biofilm growth, informs the development of predictive models of transport and mechanical properties of biofilms, and provides a method for quantifying the kinetics of bacterial surface colonization as well as biofilm fracture and fragmentation.



## 1. INTRODUCTION

Bacterial biofilms are multicellular, surface-adherent, structured communities of cells encapsulated in a polysaccharide matrix. Biofilm formation occurs when bacteria shift from a planktonic phenotype to a sessile phenotype—an observable trait resulting from an organism's gene regulation, environmental factors, and interactions between the two. These bacterial communities are known to be structurally heterogeneous<sup>1–3</sup> and are found in a variety of clinical, industrial, and environmental settings. Biofilms can be viewed as a biocolloidal composite material consisting of bacterial cells as the colloidal particles, and matrix materials such as polyintercellular adhesion (PIA), proteins and DNA as the viscoelastic hydrogel.<sup>4</sup> The interactions at the interface of these components determine the mechanical properties and behavior of the composite material, similar to the way in which the elasticity of attractive colloidal systems such as gels, networks, and glasses is determined by the statistical configuration of particles.<sup>5</sup> There is also evidence suggesting that the mechanical properties of biofilms are strongly dependent on the intercellular microstructure, primarily due to the heterogeneity of the biofilm structure.<sup>6,7</sup> Such mechanical properties and how they vary in different

environments plays an important role in the accumulation, maturation, and dispersion stages of the biofilm life cycle.<sup>4,8–10</sup>

Confocal laser scanning microscopy (CLSM) is a useful tool for quantifying the microstructure of biofilms because it provides a nondestructive method to image a 3D volume of cells within a mature, hydrated biofilm.<sup>11</sup> CLSM has previously been used to observe heterogeneity of gross morphological features during biofilm development and adaptation.<sup>12–15</sup> Because a large field of view ( $\sim 250 \times 250 \mu\text{m}^2$  or greater) is used to observe such gross morphology, the resulting images are low magnification. This low magnification does not resolve the intercellular features of the biofilm microstructure that are displayed at  $5 \mu\text{m}$  scales and smaller, and which are important to the aforementioned questions of biofilm rheology and permeability.

More recently, high-resolution CLSM methods have been identified as valuable tools to address fundamental questions about the intercellular microstructure of biofilms and their

Received: April 8, 2013

Revised: May 17, 2013

Published: May 20, 2013

components.<sup>16,17</sup> Here, we define the intercellular microstructure as the spatial organization of biofilm cells on length scales from  $\sim 0.5\ \mu\text{m}$  up to  $5.0\ \mu\text{m}$ . This scale is observable by means of high resolution CLSM imaging, which can resolve submicron features of biofilms. Moreover, analyzing biofilms at this resolution potentially quantifies morphological features mediated by the effects of cell division, extracellular matrix synthesis, and diffusive transport (e.g., of oxygen, nutrients, antibiotics, quorum sensing molecules).<sup>2</sup>

When equipped with high numerical aperture objectives, CLSM yields submicron resolution for characterizing the many body interactions at the  $0.5\text{--}5.0\ \mu\text{m}$  scale. However, quantitative analysis of the CLSM images requires image analysis methods that determine the intercellular microstructure of biofilms by characterizing cellular locations. These strategies can be adapted from work in colloidal and materials science.<sup>18–20</sup> These techniques describe structural features by determining statistical measures such as the number of bacteria per unit volume (i.e., the number density); the variation in spacing between cells; the probability of finding a bacterium at some distance from a reference bacterium (i.e., the radial distribution function); and the spatial clustering (or clumpiness) of a collection of individual cells (i.e., the cluster distribution). These measures quantify, in a statistically well-defined way, the phenotypic differences that arise among strains, species, and environmental conditions in biofilms. They also connect to a large collection of theories, tools, and techniques in the physical sciences that already exist to study materials at a microscopic level.<sup>21</sup>

Bacterial biofilm infection and surface colonization is a major complication of medical device procedures. *Staphylococcus epidermidis*, a prominent member of normal human skin flora, and a primary cause of complications for patients with medical implants,<sup>22</sup> was chosen as the model organism for our studies. As with other biofilm-associated infections, *S. epidermidis* causes disease and device failure by establishing a surface-adherent viscoelastic composite of cells and secreted polymers that resist treatment with antibiotics. As such, these living structures share much in common with other colloidal systems, a fact underscored by recent application of such methodologies to understand single cell properties,<sup>23,24</sup> and the interactions of cells with surfaces.<sup>25–27</sup> Our work extends this approach to include the multicellular properties of bacterial communities. This multicellular perspective is critical to understanding how these short-range physical and chemical properties contribute to the gross mechanical behavior of bacterial biofilms that many groups have characterized.<sup>28–30</sup>

Here, we combine CLSM with image analysis methods to locate individual bacteria with submicron resolution and, thereby, statistically characterize the microscopic structure of *S. epidermidis* biofilms. These measures specifically address the following two questions: First, what is the typical variation in *S. epidermidis* biofilm architecture at the microscale as quantified by the colloidal measures of number density, radial distribution function, and cluster distribution? Second, does treatment with environmental stressors, such as increased salinity or sublethal antibiotic dosage, affect the soft matter organization of biofilms at this short length scale through a general or stress-specific response?

## 2. MATERIALS AND METHODS

**2.1. Bacterial Biofilm Growth Conditions.** *S. epidermidis* RP62A was obtained from American Type Culture Collection (ATCC

35984). Each experiment began with an overnight culture grown in tryptic soy broth (TSB). A volume of 1 mL of the overnight culture with 9 mL of TSB with 1% glucose was injected into one channel of a  $40\ \text{mm} \times 4\ \text{mm} \times 1\ \text{mm}$  flow cell with the inlet and outlet located on opposite ends of the 4 mm flow cell width (Stovall Life Sciences, Peosta, IA), and allowed to incubate without flow at  $37\ ^\circ\text{C}$  for 1 h. Flow cells were then perfused with media at  $37\ ^\circ\text{C}$  at  $0.5\ \text{mL/min}$ ,  $\text{Re} = 4$ , which induced a shear stress of  $0.01\ \text{Pa}$  along the floor of the flow cell. These conditions were chosen to represent common non-turbulent flow regimes (e.g., venous blood, cerebral spinal fluid, urine) within the human body.<sup>31–33</sup>

Each biofilm was grown within a flow cell for 24 h with TSB and 1% glucose in the unstressed condition (86 mM NaCl) and TSB and 1% glucose with either 136 mM NaCl, 776 mM NaCl, or  $1.9\ \mu\text{g/mL}$  vancomycin growth media in the stressed conditions. Twenty-four hours was chosen as the period for growth, because after 24 h bacteria have colonized the surface and biofilms have developed well beyond the initial period of attachment.<sup>34</sup> A concentration of 1% glucose was added to all growth media, because glucose supplemented media has been shown to induce the expression of the biofilm positive phenotype of *S. epidermidis*.<sup>35,36</sup> Unadjusted TSB contains 86 mM NaCl. To induce osmotic stress, we increased TSB salinity to 136 mM NaCl (representative of human extracellular fluid) and 776 mM NaCl (4% NaCl, a concentration of NaCl known to increase the production of PIA<sup>37,38</sup>). To evaluate vancomycin-associated stress,  $1.9\ \mu\text{g/mL}$  vancomycin was used, which our preliminary results and published reports confirmed was 95% of the minimum inhibitory concentration (MIC) for RP62A.<sup>39</sup> Four different flow cell biofilms were grown for each experimental condition in separate experimental runs.

**2.2. Confocal Laser Scanning Microscopy.** After 24 h growth, biofilms were stained with  $10\ \mu\text{M}$  Syto9 (Invitrogen, Carlsbad, CA) for 60 min. From each flow cell experiment, five CLSM image volumes were obtained using a Leica SP2 CLSM instrument with a  $100\times$ , 1.4 NA, oil immersion objective lens. The excitation wavelength was 488 nm. Image volumes were of size  $30\ \mu\text{m} \times 30\ \mu\text{m}$  in the objective plane parallel to the shearing surface, and  $6\text{--}25\ \mu\text{m}$  in the direction perpendicular to the shearing surface. The latter dimension was varied to accommodate differences in the biofilm thickness. The shear surface was always the lower bound of the image volume. All image voxels were  $60\ \text{nm} \times 60\ \text{nm} \times 60\ \text{nm}$ . The five image volumes were collected in the shape of a cross, centered across the width of the flow cell. The spacing between each imaged volume was  $100\ \mu\text{m}$ , and all measurements were taken in the 10 mm nearest the flow cell inlet. We image near the center of the inlet to ensure nutrient depletion has not occurred as flow traverses the length of the flow cell and to require that we have minimal effects of flow instabilities that commonly exist at the corners of the expansion flow into the cell.

**2.3. Image Analysis.** Image analysis of raw CLSM image stacks was performed to determine the collective structure of the biofilm. Our image processing resolves the spatial position of all bacteria within each image volume with sub-100 nm resolution. The method, based on the work of Crocker and Grier,<sup>18</sup> resolves the location of all bacterium geometric centroids within an image volume to within  $\pm 35\ \text{nm}$  in the object plane and  $\pm 45\ \text{nm}$  in the axial plane.<sup>19</sup> The error of statistical measures from the image analysis, such as the number density, is less than 3%.<sup>40</sup> This method inputs raw image data, filters out noise through the use of a Gaussian mask, identifies the brightest voxel in a local region of width,  $w$ , and then corrects for bacterium location error. The performance on the method was verified by confirming that all bacteria were correctly identified within subregions of an image volume. Results for one such subregion are reported in Figure 1. The 3D coordinates of all the bacteria in the image volume were rendered in POV-Ray, a ray-tracing program (POV-Ray, Persistence of Vision Raytracer [<http://www.povray.org>]).

**2.4. Quantification of Spatial Organization.** The local number density, the cluster distribution, the radial distribution function, and the dimensionality of fractal structures were determined from the coordinates of the identified bacteria. The local number density is the number of bacteria per unit volume within the imaged region of the biofilm.

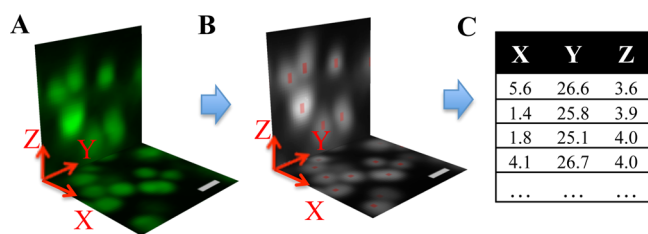


**Figure 1.** Determination of bacterium centroid locations using CLSM coupled with image analysis. (A) Two perpendicular image sections taken from the 3D CLSM image volume. (B) Bacterium centroid locations identified within the two perpendicular image slices by image processing. Centroids are indicated in red. (C) List of centroid coordinates (in  $\mu\text{m}$ ) identified in (B). Scale bars:  $1 \mu\text{m}$ .

To quantify spatial clustering, all cells in an imaged volume were grouped according to the following definition: (i) all members of a group were separated from at least one other member of the group by no more than a critical distance  $r_c$ , the cluster cutoff distance; (ii) each member of a group was separated from all other members of all other groups by at least that same critical distance  $r_c$ . That is, all bacteria in a cluster share at least one link with another bacteria within the same cluster, and no links with bacteria in other clusters. The definition is shown figuratively in Figure 5a. Clusters were identified according to the method of Lu et al.<sup>41</sup> The cluster distribution was reported as the ratio of the number of clusters for a given  $r_c$  to the total number of bacteria within the image volume.

The radial distribution function, a common structural measure from statistical mechanics, is defined as the probability of finding a bacterium at a distance,  $r$ , from a reference bacterium at the origin. It is computed as in Allen and Tildesley.<sup>42</sup>

For phenotypes with fractal structure, the fractal dimension,  $d_f$ , was determined by a power-law fit of the average radial distribution function from  $2R < r < 10R$ , where  $R$  is  $320 \text{ nm}$ , the average radius of *S. epidermidis* RP62A.<sup>43</sup> In this region, the radial distribution function is related to the fractal dimension through the relationship,  $g(r) \sim r^{d_f-3}$ .<sup>44,45</sup>

**2.5. Statistical Analysis.** Bacterial number density results were analyzed with one-way ANOVA when examining differences between different levels of osmotic stress. Vancomycin effects were compared to the  $86 \text{ mM}$  NaCl condition with unpaired  $t$  tests. Comparison of the clustering and radial distribution functions between experimental groups was carried out using spline-based general additive models as used previously for spatial characterization of bacterial aggregate geometry,<sup>16</sup> and as outlined in the *mgcv* package in R 2.15.1 (Wood, S., R Foundation for Statistical Computing [http://www.r-project.org/index.html]).

### 3. RESULTS

Unstressed *S. epidermidis* biofilms grown in flow cells exhibited heterogeneous structure on multiple length scales, as reported in Figure 2. Figure 2A shows the heterogeneity across the width of the flow cell at the millimeter length scale, as indicated by stereoscopic imaging. Figure 2B shows the spatial heterogeneity observed when using a  $10\times$ ,  $0.3 \text{ NA}$  objective; Figure 2C shows the spatial heterogeneity when using a  $40\times$ ,  $0.95 \text{ NA}$  objective. The images indicate that these biofilms, consistent with the literature,<sup>12–15</sup> display a hierarchy of structures of dimension  $200 \mu\text{m}$  and smaller. Using  $10\times$  microscopy and COMSTAT,<sup>14</sup> we find that the unstressed biofilm thickness is  $\sim 200 \mu\text{m}$  and that the available biovolume is  $\sim 90 \mu\text{m}^3/\mu\text{m}^2$ .

Here we probe a finer length scale, and thereby show that *S. epidermidis* biofilm architecture is heterogeneous at scales  $< 5 \mu\text{m}$ , as shown in Figure 2D. This length scale of our 3D imaging is an order of magnitude smaller than those typically reported for biofilm images. Figure 2C is a single image slice from an image volume used for image processing. Figure 2E shows renderings of all bacterial centroids identified within the entire CLSM volume that the slice in Figure 2D was taken from. These centroids were used to quantify intercellular biofilm structural heterogeneity. CLSM, at these short length scales ( $< 5 \mu\text{m}$ ), revealed highly varied cellular density in healthy, unstressed *S. epidermidis* biofilms. The range of local number densities varied significantly with local number densities varying from  $0.02$  to  $0.41 \text{ cells}/\mu\text{m}^3$ , and with a mean of  $0.19 \pm 0.03 \text{ cells}/\mu\text{m}^3$ .

Bacterial local number densities decreased with increased osmotic stress, an environmental stress added to the growth environment of the bacteria. The average local number density decreased to  $0.09 \pm 0.01 \text{ cells}/\mu\text{m}^3$  for biofilms grown in  $136 \text{ mM}$  NaCl, and further decreased to  $0.020 \pm 0.003 \text{ cells}/\mu\text{m}^3$  for biofilms grown in  $776 \text{ mM}$  NaCl. Thus, high osmotic stress decreased average bacteria local number density 10-fold.

The variability of the range of local number densities also decreased as osmotic stress increased. Plotting histograms of the data reveals this decrease in variability, as reported in Figure 3. As demonstrated by the variation in these plots, heterogeneity in local number density is apparent within all osmotic stress conditions; however, high-density regions of growth are excluded as stress is increased as represented by the decrease in number of bins. Although high cellular densities are not achieved with added stressors, biofilm growth is still

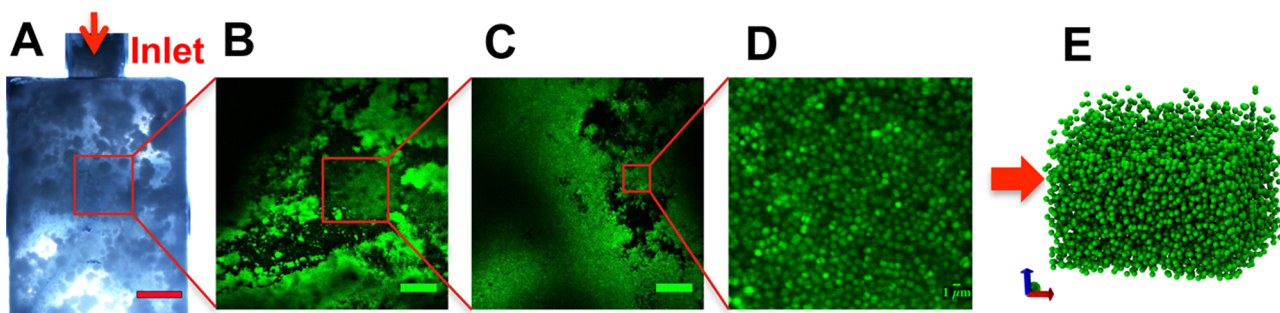


**Figure 2.** Multiscale structure of *S. epidermidis* biofilms. (A) Stereoscope image of heterogeneous biofilm structure across flow cell inlet. Flow through the device results in a wall shear stress of  $0.01 \text{ Pa}$ . Scale bar:  $1 \text{ mm}$ . (B) Single slice of a large microscale,  $1270 \mu\text{m} \times 1270 \mu\text{m} \times 224 \mu\text{m}$  CLSM image volume taken with a  $10\times$ ,  $0.3 \text{ NA}$  objective. Scale bar:  $200 \mu\text{m}$ . (C) Single image of a  $317 \mu\text{m} \times 317 \mu\text{m} \times 26 \mu\text{m}$  CLSM volume at a length scale typical for gross structural studies taken with a  $40\times$ ,  $0.95 \text{ NA}$  objective. Scale bar:  $50 \mu\text{m}$ . (D) Single CLSM slice from 3D image volume of *S. epidermidis* biofilm rendered in panel (E). Scale bar:  $1 \mu\text{m}$ . (E) 3D rendering of bacterial coordinates representing the 3D intercellular microstructure of the entire volume from image section of D.



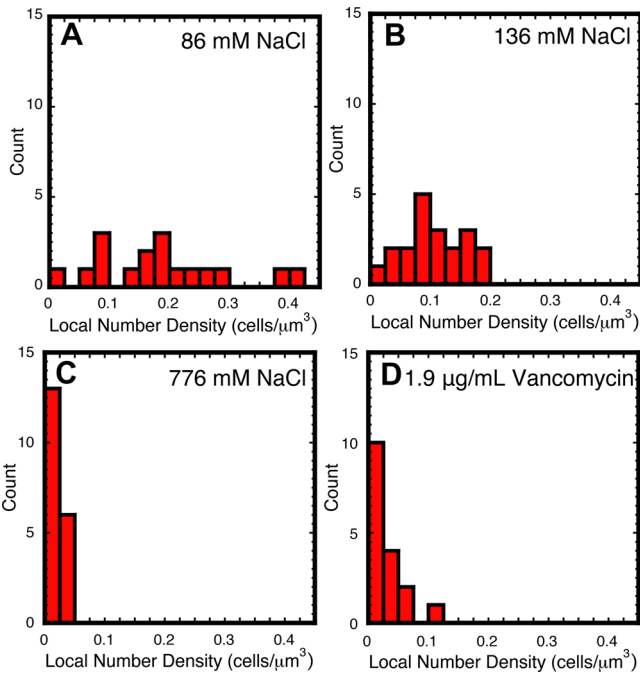


**Figure 3.** Heterogeneity of number densities decreases with increasing environmental stress. Histograms of local number density data for (A) 86 mM NaCl, (B) 136 mM NaCl, (C) 776 mM NaCl, and (D) 1.9  $\mu\text{g/mL}$  vancomycin.

present. This observation indicates that PIA or other matrix components contribute significantly to biofilm formation when environmental stressors are present. Therefore, the control variable of osmotic stress is able to induce differences in biofilm cellular morphology. Numerical values of averages and ranges at the different stress conditions studied are reported in Table 1.

**Table 1.** Average Local Number Density Values and Range of Local Number Density Values for Each Growth Condition

Environmental Condition	Average Local Number Density ( $\text{cells}/\mu\text{m}^3$ )	Range of Local Number Densities ( $\text{cells}/\mu\text{m}^3$ )
86 mM NaCl	$0.19 \pm 0.03$	0.02–0.41
136 mM NaCl	$0.09 \pm 0.01$	0.02–0.19
776 mM NaCl	$0.02 \pm 0.003^a$	0.005–0.04
1.9 $\mu\text{g/mL}$ vancomycin	$0.02 \pm 0.006^b$	0.003–0.11

<sup>a</sup> $p < 0.01$  for increasing salinity by one-way ANOVA. <sup>b</sup> $p < 0.01$  for vancomycin versus 86 mM NaCl by unpaired  $t$  test.

Bacterial local number densities decreased with vancomycin stress. With a sublethal vancomycin stress, the average local number density is  $0.02 \pm 0.01 \text{ cells}/\mu\text{m}^3$ . However, and as indicated by the histograms in Figure 2D, the variability in local number densities decreased, compared to the unstressed growth condition, when stressed with vancomycin. Thus, we found that both osmotic and sublethal vancomycin stress decreased average local number density of cells within the biofilm, but did not eradicate biofilm growth.

Three general density phenotypes—low (Density Phenotype I), medium (Density Phenotype II), and high (Density Phenotype III) local number density phenotypes—were identified. Due to the variation in local number densities present in unstressed biofilms, we categorized the measured local number densities into three density phenotype regions:

the low-density phenotype (I) is from 0 to  $0.06 \text{ cells}/\mu\text{m}^3$ ; the medium density phenotype (II) is from  $0.06$  to  $0.20 \text{ cells}/\mu\text{m}^3$ ; and the high-density phenotype (III) is from  $0.20$  to  $0.41 \text{ cells}/\mu\text{m}^3$ . We established the range of each phenotype by considering the entire range of local number densities that could be achieved by both unstressed and stressed biofilms and empirically determining two divisions within the data. The first division was the maximum density observed at the most stressed condition of 776 mM NaCl, which was about  $0.06 \text{ cells}/\mu\text{m}^3$ . This limit was taken as the upper bound of the low-density phenotype for all conditions. The second division was taken as the density range in which only the unstressed biofilms (86 mM NaCl) displayed biofilm growth. This limit ( $0.20 \text{ cells}/\mu\text{m}^3$ ) was taken as the lower limit of the high-density phenotype. The difference between these two limits was the medium density phenotype. These limits were applied uniformly to all four environmental growth conditions.

The density phenotype ranges are plotted on a per sample basis in Figure 4A. In Figure 4A, different symbols denote each

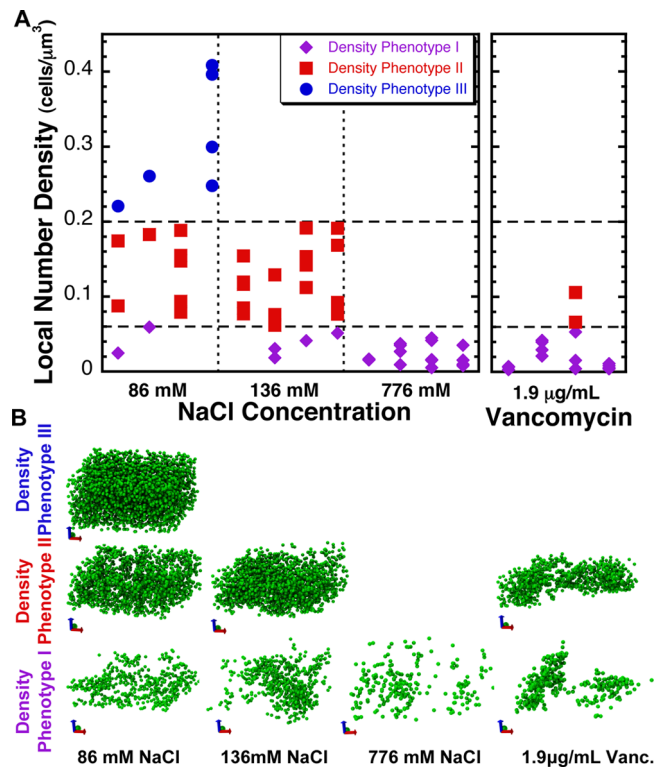


**Figure 4.** (A) Bacterial local number density varies according to environmental stress condition and can be described by identification of three density phenotypes. Within each condition, each column of data represents the results of one flow cell replicate. There were four replicates per experimental condition. (B) Representative 3D renderings of bacteria, organized by both environmental stress condition and low (I), medium (II), and high (III) density phenotypes. As osmotic stress increased, the number of density phenotypes present decreased.

of the three density phenotypes. Three-dimensional projections of bacterial centroids extracted from representative CLSM image volumes from each condition for each phenotype are shown in Figure 4B. The low-density phenotype exhibits more clustering than the medium- and high-density phenotypes. The medium- and high-density phenotypes are qualitatively more close-packed and more uniform than the low-density

phenotypes. As stress is increased within the system, fewer phenotypes are present.

Cluster distributions indicated that all *S. epidermidis* biofilm phenotypes contain close spatial association at short length scales, presumably due to daughter cells from cell division. The cluster distribution, plotted in Figure 5B, shows that similarities exist in *S. epidermidis* biofilm clustering for all density phenotypes at short length scales ( $r_c < \sim 1.0 \mu\text{m}$ ). This conclusion is drawn from the fact that a sharp decrease in the ratio of number of clusters to total number of bacteria (the y-axis in Figure 5B) occurs at a cluster cutoff,  $r_c$ , of  $\sim 1 \mu\text{m}$ . This sharp decrease is at the same length scale as that expected for the effects of cell division. That is, at the separation distance of daughter cells (dimers) and pairs of daughter cells (tetramers), the number of clusters drops precipitously. This drop occurs because on the  $1 \mu\text{m}$  scale bacteria are grouped together into dimers and tetramers. These dimer and tetramer groups suggest that the biofilm density phenotypes found have internal structure seemingly linked to cell division. Representative sections of CLSM images of dimers, trimers, and tetramers found in the biofilms are shown in Figure 5C.

Cluster distributions showed that cellular connectivity at  $r_c = 6 \mu\text{m}$  is a strong function of density phenotype. In the limit of  $r_c > 2 \mu\text{m}$ , the low-density phenotype contains significantly more clusters relative to that of the medium and high-density phenotypes, as shown on the right-hand side of Figure 5B. Increased clustering of the low-density phenotype is indicated by the fact that the ratio of number of clusters to number of bacteria ( $N_{\text{Cl}}/N_{\text{B}}$ ) only decreases to 0.04 at  $r_c = 6 \mu\text{m}$ , instead of dropping to nearly 0 ( $< 10^{-3}$ ) as in the medium and high density phenotypes.  $N_{\text{Cl}}/N_{\text{B}}$  tending to zero indicates that all bacteria in the image volume have been grouped into either a single cluster, or a few very large clusters (typically  $> 1000$  bacteria/cluster).

Thus, in the low-density phenotype, biofilms are structured at  $\sim 6 \mu\text{m}$  scales into small clusters of abundance equal to about 4% of the total number of cells. In the medium- and high-density phenotypes cells on this scale are connected into large clusters that span the entire image volume.

The radial distribution function corroborates the short-range structural findings of the cluster analysis. The radial distribution function,  $g(r)$ , is the probability of finding a bacterium at a distance,  $r$ , given that a reference bacterium is located at the origin, relative to a uniform distribution of the same density. Thus, peaks in the radial distribution function represent an increased probability of finding a bacterium at a given location from the origin, while troughs represent a decrease in the probability of finding a bacterium at a given location from the origin. The radial distribution functions plotted in Figure 5D display two features that corroborate the cluster distribution findings.

First, the radial distribution function of each density phenotype displays a peak at short length scales ( $< 1.2 \mu\text{m}$ ). This peak indicates an increased probability of finding bacteria separated by short distances relative to a uniform distribution of bacteria. These peaks support the evidence of a first coordination shell on the length scale of cell division in the biofilms.

Second, the magnitude of the radial distribution function of the low-density phenotype is significantly greater than the medium- and high-density phenotypes. The medium- and high-density phenotype measurements are consistent with results for disordered liquids and packings, such as those found in fluid

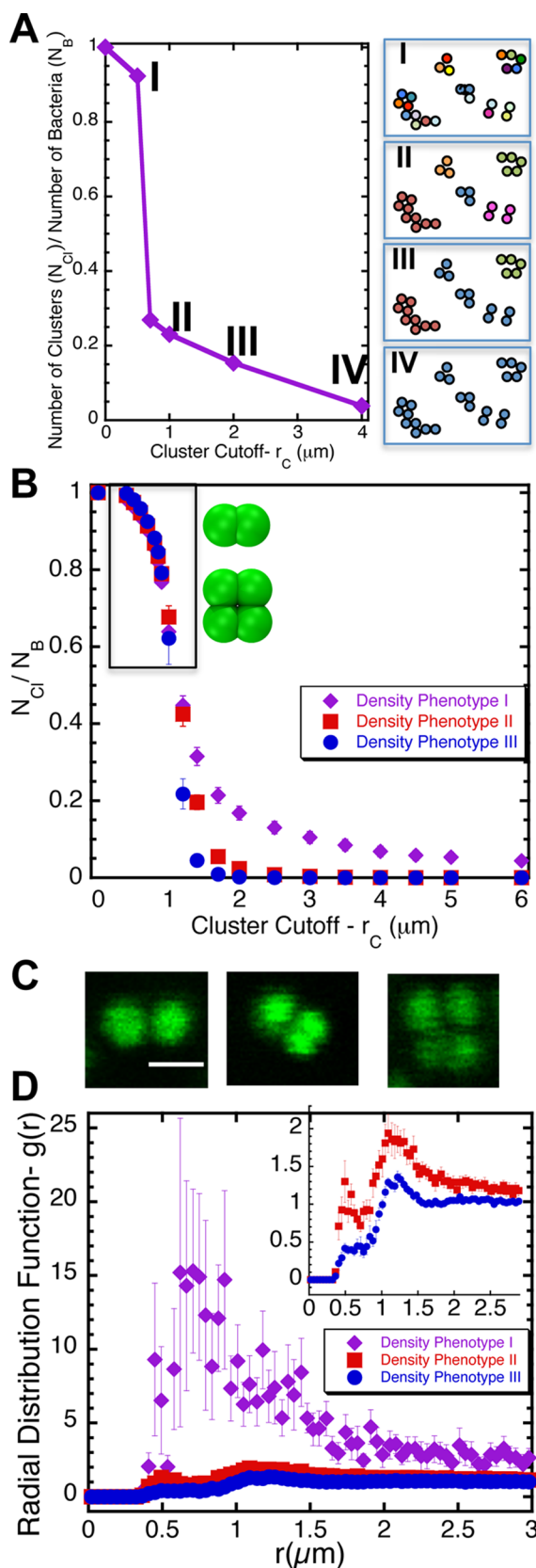


**Figure 5.** (A) Schematic representations of specific regions within the cluster distribution curve. When the cluster cutoff size,  $r_c$ , is low, the number of bacteria in each cluster is low. This decrease results from the close spatial association required by small  $r_c$ . Thus, many clusters are identified, each with few bacteria. Conversely, when  $r_c$  is high, bacteria are increasingly connected and the number of clusters is small.

Figure 5. continued

In the above figure each cluster is represented by a different color. (I)  $r_c = 0.5 \mu\text{m}$  shows that all cells other than the pair of cells in the middle that are directly touching are counted as individual clusters. (II)  $r_c = 0.7 \mu\text{m}$  yields 5 clusters. (III)  $r_c = 1 \mu\text{m}$  yields 3 clusters. (IV)  $r_c = 4 \mu\text{m}$  yields one cluster. (B) Cluster distribution of low (I), medium (II), and high (III) density phenotypes. Cluster distribution is plotted as number of clusters ( $N_{\text{Cl}}$ )/number of bacteria ( $N_{\text{B}}$ ) versus cluster cutoff ( $r_c$ ). All biofilms cluster at  $r_c \sim 1 \mu\text{m}$  indicating that all growth conditions and density phenotypes contain similar clustering on length scales of cell division (upper left-hand box). This clustering consists of small clusters: dimers, trimers, and tetramers. In addition, cluster distributions for  $r_c \sim 5 \mu\text{m}$  differ in cellular connectivity between the low-density phenotypes and the medium- and high-density phenotypes. A greater number of clusters (equal to  $\sim 4\%$  of the number of cells) are present within the low-density phenotype (I) compared to the medium(II)- and high(III)-density phenotypes, where only single clusters are present at  $\sim 6 \mu\text{m}$  for these two cases. The cluster distribution data analyzed include all data collected from both unstressed and stressed biofilms with the given phenotype. All curves for the three phenotypes were statistically distinct by general additive modeling ( $p < 0.01$  for each). (C) CLSM evidence of clustering of dimers, trimers and tetramers, on length scales linked to cell division. Scale bar:  $1 \mu\text{m}$ . (D) Radial distribution function of low (I), medium (II), and high (III) density phenotypes. The peaks at  $< 1.2 \mu\text{m}$  indicate that bacteria are separated by short distances, consistent with the short-range clustering of panel (A). Additionally, the significantly higher peak of the low(I)-density phenotype indicates fractal structure of the biofilm, whereas the peaks of the medium(II)- and high(III)-density phenotypes indicate dense, disordered packing of the biofilm. The  $g(r)$  data analyzed include all data collected from both unstressed and stressed biofilms with the given phenotype. All curves for the three phenotypes were statistically distinct by general additive modeling ( $p < 0.01$  for each).

and glassy suspensions of colloids.<sup>46</sup> By comparison, the large magnitude of the radial distribution function of the low-density phenotype indicates substantial deviation in bacterial pair separation relative to that expected for a uniform distribution of bacteria. This heterogeneity is consistent with the both the greater clumpiness on  $\sim 6 \mu\text{m}$  length scales found in the cluster distribution of low-density phenotypes, and the colloidal clustering of structures with fractal distributions.<sup>47</sup> To further understand the low-density phenotype, we quantified the fractal behavior of these structures (over the range  $2R < r < 10R$ ), and determined the average fractal dimension to be  $1.7 \pm 0.1$ . Although the mechanism of association is potentially very different, it is interesting that this value is similar to the Diffusion Limited Cluster Aggregation (DLCA) regime, for which  $d_f = 1.8$ .<sup>48</sup> A plot of the data and fit used to determine the fractal dimension is shown in Supporting Information Figure 1.

#### 4. DISCUSSION

This paper has applied high-resolution confocal laser scanning microscopy coupled with image analysis to evaluate the effect of environmental stress and antibiotics on biofilm architecture on the  $0.5\text{--}5 \mu\text{m}$  scale of intercellular microstructure. Our findings indicate that unstressed *S. epidermidis* biofilm architecture is highly variable at short length scales, consisting of distinct phenotypes distributed across the biofilm. In unstressed biofilms, the cellular density of these phenotypes varies by a factor of 20. Osmotic stress decreased the variation in number density of *S. epidermidis* biofilms, as indicated by the uniformly

low local number densities of these samples. Likewise, stress from vancomycin, an antibiotic commonly used to treat staphylococcal infections, reduced the structural variation of the biofilms, as shown by an equivalent decrease in the range of the local number density phenotypes present.

We probed the internal structure of the high-, medium-, and low-density phenotypes through cluster distribution analysis. We found that low-density phenotypes consisted of small clusters of bacteria, whereas high-density phenotypes displayed continuous connectivity throughout the entire volume being sampled. We also found that all biofilms observed contained short-range structure on length scales commensurate with cell division.

This work demonstrates that clustering of low-density biofilms on scales of  $\sim 6 \mu\text{m}$  and below is a common feature of biofilms. We observed increased clustering of *S. epidermidis* in low-density phenotype biofilms on length scales  $< 6 \mu\text{m}$ . This scale is similar to clustering observed by Berk et al. in *Vibrio cholerae* biofilms.<sup>17</sup> The observation of such clustering in two different biofilm forming species suggests that the  $\sim 6 \mu\text{m}$  scale is broadly relevant to understanding the morphology and architecture of bacterial biofilms. Moreover, as discussed in the next paragraphs, our work extends the understanding of this clustering by showing (a) unstressed biofilms have cellular connectivity across  $\sim 30 \mu\text{m}$  regions, while stressed biofilms only maintain cellular connectivity on  $\sim 6 \mu\text{m}$  size scales; (b) small scale clustering in biofilms is consistent with the effects of cell division; and (c) low-density biofilms form fractal structures with fractal dimensions  $d_f = 1.7 \pm 0.1$ .

The long-range ( $\sim 30 \mu\text{m}$ ) cellular connectivity of unstressed biofilms with high- and medium density phenotypes and the short-range cellular connectivity of stressed biofilms ( $\sim 6 \mu\text{m}$ ) with low-density phenotypes have implications for the mechanism of biofilm connectivity in each of these systems. The cluster distribution characterization of Figure 4A distinguishes between cells that are directly connected to each other (because they are separated by distances  $< 5 \mu\text{m}$  and thus grouped into a single cluster), and cells that are not directly connected, and thus are associated indirectly through PIA and other components of the EPS (because the cells are separated by distances greater than  $6 \mu\text{m}$ ). This finding shows that cellular connectivity in stressed biofilms is decreased relative to unstressed biofilms. This difference in cellular contact and connectivity may have implications for the rheological (e.g., elastic modulus, yield strength) and transport properties (e.g., diffusion of oxygen, nutrients, antibiotics, quorum sensing molecules) of biofilms. For example, the bacterial contact interactions could deform with a rigid or soft response depending on the spacing and angles between bacteria. These two types of clusters would behave differently when subjected to deformation.<sup>49,50</sup>

Cell replication also appears to significantly impact biofilm microstructure. Both unstressed biofilms and biofilms grown in the presence of environmental stressors contained structure signatures suggestive of cell division on length scales of  $< 2 \mu\text{m}$ . This result suggests that progeny remain nearby original cells within biofilms.

Low-density phenotype *S. epidermidis* biofilms have an average fractal dimension ( $d_f = 1.7 \pm 0.1$ ) consistent with values found for other modes of aggregation, such as diffusion limited cluster aggregation.<sup>51</sup> This tenuous structure of the low-density phenotype biofilms is similar to that observed for number of of colloidal gels<sup>52</sup> formed through spinodal



decomposition-type mechanisms. The mechanism of bacteria clustering into fractal structures is likely more complex than such colloidal mechanisms of aggregation because of the potential contribution of cell division, matrix materials, and quorum sensing to the multicellular structure of bacterial communities. Nevertheless, the very low fractal dimension observed is consistent with the very open, low dimensionality structures for these loose biofilms. The fractal structure of gels has profound implications for rheological properties; for example, in colloidal systems, both the fractal structure and cluster dimension specify the hierarchy of fluctuating modes that determine the gel elasticity.<sup>53</sup> Identification of this structural feature in stressed biofilms suggests a potential avenue to model the contribution of their intercellular structure to their elastic rheology. In colloidal gels, fractal models of internal particle dynamics have been used to develop a scaling relationship among the volume fraction, fractal dimension, and elastic modulus.<sup>53</sup> Similar scaling relationships may be useful for determining the elastic moduli of biofilms.

More broadly, the experimental characterization of the spatial position of every bacterium in a local region of the biofilm, as pursued in the present study, is critical to advancing understanding of a number of biofilm transport and mechanical properties. For example, spatial coordinates can be used to further understand matrix behavior through allowing for calculations of the average extracellular concentration of PIA per cell present within the biofilm.<sup>43</sup> Moreover, the bacterial positions can be applied to initialize composite based predictive models of biofilm mechanical behavior, thereby better linking these models to real conditions in the biofilms. These models have been applied to flow induced fragmentation models of biofilms.<sup>54</sup> Additionally, computer modeling of biofilms has shown how clustering behavior may change due to social evolution within single species and multi-species biofilms.<sup>55</sup> Consequently, the tools developed in the present study are immediately applicable for experimentally evaluating the behavior of each individual species in these simulations or could be expanded to multi-species biofilms for testing the structural behavior of each species as well.

## 5. CONCLUSIONS

Our work has identified that unstressed biofilms are comprised of multicellular structures representing the full range of high-, medium-, and low-density phenotypes, while biofilms stressed by either osmotic pressure or an antibiotic contain only medium- and low-density phenotypes. Although it was expected that biofilms undergoing stress would not develop as extensively as unstressed biofilms, the short- and long-range structural behaviors that accompany these developmental differences were previously unknown. All *S. epidermidis* biofilms observed contained clustering commensurate with the length scale of cell division ( $\sim 1 \mu\text{m}$ ). However, biofilm connectivity differed on  $\sim 6 \mu\text{m}$  scales, where high- and medium-density phenotype biofilms contained longer range connectivity ( $>30 \mu\text{m}$ ), and low-density phenotype biofilms clustered into fractal structures. Advancing the understanding of how bacteria organize at the intercellular level in unstressed and stressed conditions introduces a new perspective for understanding biofilm growth. The metrics used here could be applied to quantify and advance the understanding of the kinetics of bacterial surface colonization in both single species and multispecies biofilms, bacterial behavior at the biofilm–water

interface or other regions within the biofilm, and biofilm dispersal, fracture, and fragmentation.

## ■ ASSOCIATED CONTENT

### Supporting Information

Supplementary Figure 1: Fractal dimension calculation. This material is available free of charge via the Internet at <http://pubs.acs.org>.

## ■ AUTHOR INFORMATION

### Corresponding Author

\*Fax: 734-763- 0459. Tel: 734-764-3119. E-mail: [mjsolo@umich.edu](mailto:mjsolo@umich.edu).

### Author Contributions

The manuscript was written through contributions of all authors. All authors have given approval to the final version of the manuscript.

### Notes

The authors declare no competing financial interest.

## ■ ACKNOWLEDGMENTS

This work was supported by the National Science Foundation Graduate Research Fellowship program, the NSF CDI (Grant PHYS-0941227), and the NIGMS division of NIH (Grant GM-069438). The authors would like to thank R. Newman and L. C. Hsiao for the use of their cluster distribution program.

## ■ REFERENCES

- (1) Costerton, J. W.; Stewart, P. S.; Greenberg, E. P. Bacterial biofilms: a common cause of persistent infections. *Science* **1999**, *284*, 1318.
- (2) Stewart, P. S.; Franklin, M. J. Physiological heterogeneity in biofilms. *Nat. Rev. Microbiol.* **2008**, *6*, 199–210.
- (3) Fux, C. A.; Costerton, J. W.; Stewart, P. S.; Stoodley, P. Survival strategies of infectious biofilms. *Trends Microbiol.* **2005**, *13*, 34–40.
- (4) Wilking, J. N.; Angelini, T. E.; Seminara, A.; Brenner, M. P.; Weitz, D. A. Biofilms as complex fluids. *MRS Bull.* **2011**, 36.
- (5) Zaccarelli, E. Colloidal gels: Equilibrium and non-equilibrium routes. *J. Phys.: Condens. Matter* **2007**, *19*, 323101.
- (6) Hohne, D. N.; Younger, J. G.; Solomon, M. J. Flexible Microfluidic Device for Mechanical Property Characterization of Soft Viscoelastic Solids Such as Bacterial Biofilms. *Langmuir* **2009**, *25*, 7743–7751.
- (7) Rogers, S. S.; van, d. W., C.; Waigh, T. A. Microrheology of Bacterial Biofilms In Vitro: *Staphylococcus aureus* and *Pseudomonas aeruginosa*. *Langmuir* **2008**, *24*, 13549–13555.
- (8) Hall-Stoodley, L.; Costerton, J. W.; Stoodley, P. Bacterial biofilms: from the Natural environment to infectious diseases. *Nat. Rev. Microbiol.* **2004**, *2*, 95–108.
- (9) Lieleg, O.; Caldara, M.; Baumgärtel, R.; Ribbeck, K. Mechanical robustness of *Pseudomonas aeruginosa* biofilms. *Soft Matter* **2011**, *7*, 3307–3314.
- (10) Aggarwal, S.; Poppele, E. H.; Hozalski, R. M. Development and testing of a novel microcantilever technique for measuring the cohesive strength of intact biofilms. *Biotechnol. Bioeng.* **2010**, *105*, 924–934.
- (11) Dunne, W. M., Jr. Bacterial adhesion: seen any good biofilms lately? *Clin. Microbiol. Rev.* **2002**, *15*, 155.
- (12) Xavier, J. B.; White, D. C.; Almeida, J. S. Automated biofilm morphology quantification from confocal laser scanning microscopy imaging. *Water Sci. Technol.* **2003**, *47*, 31–37.
- (13) Beyenal, H.; Donovan, C.; Lewandowski, Z.; Harkin, G. Three-dimensional biofilm structure quantification. *J. Microbiol. Methods* **2004**, *59*, 395–413.
- (14) Heydorn, A.; Nielsen, A. T.; Hentzer, M.; Sternberg, C.; Givskov, M.; Ersbøll, B. K.; Molin, S. Quantification of biofilm

structures by the novel computer program COMSTAT. *Microbiology* **2000**, *146*, 2395.

(15) McLean, J. S.; Ona, O. N.; Majors, P. D. Correlated biofilm imaging, transport and metabolism measurements via combined nuclear magnetic resonance and confocal microscopy. *ISME J.* **2007**, *2*, 121–131.

(16) Dzul, S. P.; Thornton, M. M.; Hohne, D. N.; Stewart, E. J.; Shah, A. A.; Bortz, D. M.; Solomon, M. J.; Younger, J. G. Contribution of the *Klebsiella pneumoniae* Capsule to Bacterial Aggregate and Biofilm Microstructures. *Appl. Environ. Microbiol.* **2011**, *77*, 1777–1782.

(17) Berk, V.; Fong, J. C. N.; Dempsey, G. T.; Develioglou, O. N.; Zhuang, X.; Liphardt, J.; Yildiz, F. H.; Chu, S. Molecular Architecture and Assembly Principles of *Vibrio cholerae* Biofilms. *Science* **2012**, *337*, 236–239.

(18) Crocker, J. C.; Grier, D. G. Methods of digital video microscopy for colloidal studies. *J. Colloid Interface Sci.* **1996**, *179*, 298–310.

(19) Dibble, C. J.; Kogan, M.; Solomon, M. J. Structure and dynamics of colloidal depletion gels: Coincidence of transitions and heterogeneity. *Phys. Rev. E* **2006**, *74*, 041403.

(20) Poon, W. C. K.; Weeks, E. R.; Royall, C. P. On measuring colloidal volume fractions. *Soft Matter* **2012**, *8*, 21–30.

(21) Dill, K. A.; Bromberg, S. Molecular driving forces: statistical thermodynamics in chemistry and biology. **2003**.

(22) Uçkay, I.; Pittet, D.; Vaudaux, P.; Sax, H.; Lew, D.; Waldvogel, F. Foreign body infections due to *Staphylococcus epidermidis*. *Ann. Med.* **2009**, *41*, 109–119.

(23) Gaboriaud, F.; Gee, M. L.; Strugnelli, R.; Duval, J. F. L. Coupled Electrostatic, Hydrodynamic, and Mechanical Properties of Bacterial Interfaces in Aqueous Media. *Langmuir* **2008**, *24*, 10988–10995.

(24) Camesano, T. A.; Natan, M. J.; Logan, B. E. Observation of Changes in Bacterial Cell Morphology Using Tapping Mode Atomic Force Microscopy. *Langmuir* **2000**, *16*, 4563–4572.

(25) Xu, H.; Murdaugh, A. E.; Chen, W.; Aidala, K. E.; Ferguson, M. A.; Spain, E. M.; Núñez, M. E. Characterizing Pilus-Mediated Adhesion of Biofilm-Forming *E. coli* to Chemically Diverse Surfaces Using Atomic Force Microscopy. *Langmuir* **2013**, *29*, 3000–3011.

(26) Emerson, Bergstrom, T. S.; Liu, Y.; Soto, E. R.; Brown, C. A.; McGimpsey, W. G.; Camesano, T. A. Microscale Correlation between Surface Chemistry, Texture, and the Adhesive Strength of *Staphylococcus epidermidis*. *Langmuir* **2006**, *22*, 11311–11321.

(27) Busscher, H. J.; van de Belt-Gritter, B.; Dijkstra, R. J. B.; Norde, W.; van, d. M.; Henny, C. *Streptococcus mutans* and *Streptococcus intermedius* Adhesion to Fibronectin Films Are Oppositely Influenced by Ionic Strength. *Langmuir* **2008**, *24*, 10968–10973.

(28) Pavlovsky, L.; Younger, J. G.; Solomon, M. J. In situ rheology of *Staphylococcus epidermidis* bacterial biofilms. *Soft Matter* **2013**, *9*, 122–131.

(29) Shaw, T.; Winston, M.; Rupp, C. J.; Klapper, I.; Stoodley, P. Commonality of Elastic Relaxation Times in Biofilms. *Phys. Rev. Lett.* **2004**, *93*, 098102.

(30) Towler, B. W.; Rupp, C. J.; Cunningham, A. L. B.; Stoodley, P. Viscoelastic Properties of a Mixed Culture Biofilm from Rheometer Creep Analysis. *Biofouling* **2003**, *19*, 279–285.

(31) McMillan, D. E. Hemorheology: Principles and Concepts. In *Levin and O'Neal's the Diabetic Foot*, 7th ed.; Bowker, J. H., Pfeifer, M. A., Eds.; Elsevier: Philadelphia, PA, **2008**; Chapter 4, pp 75–88.

(32) Howden, L.; Giddings, D.; Power, H.; Aroussi, A.; Vloeberghs, M.; Garnett, M.; Walker, D. Three-dimensional cerebrospinal fluid flow within the human ventricular system. *Comput. Methods Biomech. Biomed. Eng.* **2008**, *11*, 123–133.

(33) Lykoudis, P. S.; Roos, R. The fluid mechanics of the ureter from a lubrication theory point of view. *J. Fluid Mech.* **1970**, *43*, 661–674.

(34) Christensen, G. D.; Simpson, W. A.; Anglen, J. O.; Gainor, B. J. Methods for Evaluating Attached Bacteria and Biofilms. In *Handbook of Bacterial Adhesion*; An, Y. H., Friedman, R. J., Eds.; Humana Press: Totowa, NJ, **2000**; pp 213–233.

(35) Dobinsky, S.; Kiel, K.; Rohde, H.; Bartscht, K.; Knobloch, J. K.-M.; Horstkotte, M. A.; Mack, D. Glucose-Related Dissociation

between icaADBC Transcription and Biofilm Expression by *Staphylococcus epidermidis*: Evidence for an Additional Factor Required for Polysaccharide Intercellular Adhesin Synthesis. *J. Bacteriol.* **2003**, *185*, 2879–2886.

(36) Stepanović, S.; Vuković, D.; Hola, V.; Bonadventura, G. D.; Djukić, S.; Čirković, I.; Ruzicka, F. Quantification of biofilm in microtiter plates: overview of testing conditions and practical recommendations for assessment of biofilm production by staphylococci. *APMIS* **2007**, *115*, 891–899.

(37) Rachid, S.; Ohlsen, K.; Witte, W.; Hacker, J.; Ziebuhr, W. Effect of subinhibitory antibiotic concentrations on polysaccharide intercellular adhesin expression in biofilm-forming *Staphylococcus epidermidis*. *Antimicrob. Agents Chemother.* **2000**, *44*, 3357.

(38) Conlon, K. M.; Humphreys, H.; O'Gara, J. P. icaR encodes a transcriptional repressor involved in environmental regulation of ica operon expression and biofilm formation in *Staphylococcus epidermidis*. *J. Bacteriol.* **2002**, *184*, 4400.

(39) Polonio, R. E.; Mermel, L. A.; Paquette, G. E.; Sperry, J. F. Eradication of biofilm-forming *Staphylococcus epidermidis* (RP62A) by a combination of sodium salicylate and vancomycin. *Antimicrob. Agents Chemother.* **2001**, *45*, 3262.

(40) Kogan, M.; Dibble, C. J.; Rogers, R. E.; Solomon, M. J. Viscous solvent colloidal system for direct visualization of suspension structure, dynamics and rheology. *J. Colloid Interface Sci.* **2008**, *318*, 252–263.

(41) Lu, P. J.; Zaccarelli, E.; Ciulla, F.; Schofield, A. B.; Sciortino, F.; Weitz, D. A. Gelation of particles with short-range attraction. *Nature* **2008**, *453*, 499–503.

(42) Allen, M. P.; Tildesley, D. J. *Computer Simulation of Liquids*; Oxford University Press: New York, **1989**.

(43) Ganesan, M.; Stewart, E. J.; Szafranski, J.; Satorius, A.; Younger, J. G.; Solomon, M. J. Molar mass, entanglement and associations of the biofilm polysaccharide of *Staphylococcus epidermidis*. *Biomacromolecules* **2013**, *14*, 1474–1481.

(44) Dinsmore, A. D.; Prasad, V.; Wong, I. Y.; Weitz, D. A. Microscopic Structure and Elasticity of Weakly Aggregated Colloidal Gels. *Phys. Rev. Lett.* **2006**, *96*, 185502.

(45) Lattuada, M.; Wu, H.; Hasmy, A.; Morbidelli, M. Estimation of Fractal Dimension in Colloidal Gels. *Langmuir* **2003**, *19*, 6312–6316.

(46) Blaaderen, A. v.; Wiltzius, P. Real-Space Structure of Colloidal Hard-Sphere Glasses. *Sci. New Ser.* **1995**, *270*, 1177–1179.

(47) Dinsmore, A. D.; Weeks, E. R.; Prasad, V.; Levitt, A. C.; Weitz, D. A. Three-Dimensional Confocal Microscopy of Colloids. *Appl. Opt.* **2001**, *40*, 4152–4159.

(48) Lin, M. Y.; Lindsay, H. M.; Weitz, D. A.; Ball, R. C.; Klein, R.; Meakin, P. Universality in colloid aggregation. *Nature* **1989**, *339*, 360–362.

(49) Potanin, A. A. On the Computer Simulation of the Deformation and Breakup of Colloidal Aggregates in Shear Flow. *J. Colloid Interface Sci.* **1993**, *157*, 399–410.

(50) Hsiao, L. C.; Newman, R. S.; Glotzer, S. C.; Solomon, M. J. Role of isotacticity and load-bearing microstructure in the elasticity of yielded colloidal gels. *Proc. Natl. Acad. Sci. U.S.A.* **2012**, *109*, 16029–16034.

(51) Russel, W. B.; Saville, D. A.; Schowalter, W. R. Colloidal dispersions. **1992**.

(52) Carpineti, M.; Giglio, M. Spinodal-type dynamics in fractal aggregation of colloidal clusters. *Phys. Rev. Lett.* **1992**, *68*, 3327–3330.

(53) Krall, A. H.; Weitz, D. A. Internal Dynamics and Elasticity of Fractal Colloidal Gels. *Phys. Rev. Lett.* **1998**, *80*, 778–781.

(54) Hammond, J. F.; Stewart, E. J.; Younger, J. G.; Solomon, M. J.; Bortz, D. M. Spatially Heterogeneous Biofilm Simulations using an Immersed Boundary Method with Lagrangian Nodes Defined by Bacterial Locations. **2013**, arXiv preprint arXiv:1302.3663. arXiv.org e-Print archive. <http://arxiv.org/abs/1302.3663>.

(55) Mitri, S.; Xavier, J. B.; Foster, K. R. Social evolution in multispecies biofilms. *Proc. Natl. Acad. Sci. U.S.A.* **2011**, *108*, 10839–10846.